Structure, conformational stability, and enzymatic properties of acylphosphatase from the hyperthermophile Sulfolobus solfataricus

ARTICLE *in* PROTEINS STRUCTURE FUNCTION AND BIOINFORMATICS · NOVEMBER 2005

Impact Factor: 2.63 · DOI: 10.1002/prot.20703 · Source: PubMed

Structure, Conformational Stability, and Enzymatic Properties of Acylphosphatase From the Hyperthermophile *Sulfolobus solfataricus*

Alessandra Corazza,[1,2] Camillo Rosano,[3] Katiuscia Pagano,[1] Vera Alverdi,[1] Gennaro Esposito,[1,2] Cristina Capanni,[4] Francesco Bemporad,[4] Georgia Plakoutsi,[4] Massimo Stefani,[4,5]* Fabrizio Chiti,[4,5] Simone Zuccotti,[6] Martino Bolognesi,[6,7] and Paolo Viglino[1,2]

[1]*Dipartimento di Scienze e Tecnologie Biomediche, Università di Udine, Udine, Italy*
[2]*Centro di Eccellenza MATI, Università di Udine, Udine, Italy*
[3]*Istituto Nazionale Ricerca sul Cancro–IST, S.C. Biologia Strutturale, Genoa, Italy*
[4]*Dipartimento di Scienze Biochimiche, Università di Firenze, Florence, Italy*
[5]*Centro di Eccellenza DENOTHE, Università di Firenze, Florence, Italy*
[6]*Dipartimento di Fisica – INFM and Centro di Eccellenza CEBR, Università di Genova, Genoa, Italy*
[7]*Dipartimento di Scienze Biomolecolari e Biotecnologie, Università di Milano, Milan, Italy*

ABSTRACT **The structure of AcP from the hyperthermophilic archaeon *Sulfolobus solfataricus* has been determined by ^{1}H-NMR spectroscopy and X-ray crystallography. Solution and crystal structures (1.27 Å resolution, *R*-factor 13.7%) were obtained on the full-length protein and on an N-truncated form lacking the first 12 residues, respectively. The overall Sso AcP fold, starting at residue 13, displays the same βαββαβ topology previously described for other members of the AcP family from mesophilic sources. The unstructured N-terminal tail may be crucial for the unusual aggregation mechanism of Sso AcP previously reported. Sso AcP catalytic activity is reduced at room temperature but rises at its working temperature to values comparable to those displayed by its mesophilic counterparts at 25–37°C. Such a reduced activity can result from protein rigidity and from the active site stiffening due the presence of a salt bridge between the C-terminal carboxylate and the active site arginine. Sso AcP is characterized by a melting temperature, T_m, of 100.8°C and an unfolding free energy, $\Delta G^{H_2O}_{U\text{-}F}$, at 28°C and 81°C of 48.7 and 20.6 kJ mol^{-1}, respectively. The kinetic and structural data indicate that mesophilic and hyperthermophilic AcP's display similar enzymatic activities and conformational stabilities at their working conditions. Structural analysis of the factor responsible for Sso AcP thermostability with respect to mesophilic AcP's revealed the importance of a ion pair network stabilizing particularly the β-sheet and the loop connecting the fourth and fifth strands, together with increased density packing, loop shortening and a higher α-helical propensity. Proteins 2006;62:64–79.**

Key words: **^{1}H NMR spectroscopy; X-ray crystallography; protein thermostability; protein structure; *Sulfolobus solfataricus* acylphosphatase**

INTRODUCTION

The comparative analysis of the structural features, conformational stability, and biological function of homologous proteins from mesophilic and thermophilic organisms provides unique opportunities to gain insight into the molecular determinants of protein thermostability. The number of available protein structures from hyperthermophiles is rapidly increasing,[1–8] in part due to structural genomics approaches. In general, there is not a common determinant of thermostability[3]; however, the main physicochemical factors recognized to support thermostability are (1) the presence of ion-pair networks at the protein

Abbreviations: 2D, two-dimensional; AcP, acylphosphatase; BMRB, Biological Magnetic Resonance Bank; CD, circular dichroism; COSY, correlation spectroscopy; ct-Acp, common-type acylphosphatase; DLS, dynamic light scattering; Dro2-AcP, *Drosophila melanogaster* acylphosphatase; DQF-COSY, double quantum filtered correlation spectroscopy; ES/MS, electrospray mass spectrometry; FID, free induction decay; GdnHCl, guanidine hydrochloride; LC-ESI/MS, liquid chromatography electrospray mass spectrometry; MD, molecular dynamics; mt-AcP, human muscle–type acylphosphatase; NOESY, nuclear Overhauser effect spectroscopy; PCR, polymerase chain reaction; PDB, Protein Data Bank; RMSD, root-mean-square deviation; SDS-PAGE, sodium dodecyl sulfate–polyacrylamide gel electrophoresis; Sso AcP, *Sulfolobus solfataricus* acylphosphatase; TFA, trifluoroacetic acid; TLS, translation/libration/screw rotation; TOCSY, total correlation spectroscopy; TPPI, time-proportional phase incrementation.

Gly-1 and Ser0 do not belong to the Sso AcP sequence but are present as a result of the purification procedure; Sso AcP residue numbering differs from that of the mesophilic AcP's because of the extra N-terminal segment. Wherever proper, reference to the two numbering schemes has been reported.

The Supplementary Material referred to in this article can be found online at www.interscience.wiley.com/jpages/0887-3585/suppmat/

Grant sponsor: Italian MIUR; Grant numbers: 2002058218, RBNE01S29H, and RBAU015B47. Grant sponsor: European Union; Grant number: HPRN-CT-2002-00241. Grant sponsor: Istituto G. Gaslini (Genova, Italy; to M. Bolognesi). Grant sponsor: Fondazione Compagnia di San Paolo (Torino, Italy; to M. Bolognesi).

*Correspondence to: M. Stefani, Dipartimento di Scienze Biochimiche, Università di Firenze, Viale Morgagni 50, Florence 50134, Italy. E-mail: stefani@scibio.unifi.it

Received 8 March 2005; Revised 6 June 2005; Accepted 10 July 2005

Published online 14 November 2005 in Wiley InterScience (www.interscience.wiley.com). DOI: 10.1002/prot.20703

surface, the minimization of repulsive contacts, and the increase of hydrogen bonds among side-chains[3–9]; (2) the shortening of solvent-exposed protein loops[2]; (3) the increase in α-helical propensity of regions adopting an α-helical structure in the native state[10]; and (4) the increase of the overall protein molecule compactness.[2,7] Among these adaptations, the analysis of the genomes of hyperthermophiles, of orthologous sequences, and of structures of proteins belonging to the same families[1–3,8] has shown that a major stabilization mechanism in hyperthermophilic proteins is the replacement of polar residues (particularly glutamine, due to its propensity to deamidate at high temperatures) with charged residues.[8] Recently, it has also been proposed that different adaptations are operating in proteins from hyperthermophilic and thermophilic organisms, respectively,[7] due to the different effects of temperature on the strength of the hydrophobic or Coulombic interactions.[4,11–14] In general, such structural adaptations are mirrored by the different content of specific amino acids in homologous proteins from mesophilic and hyperthermophilic organisms.

The large increase in the number of available structures of proteins from hyperthermophiles has not been matched by a comparable wealth of data on the thermodynamics and kinetics of thermostable protein folding. In general, an increased structural rigidity of hyperthermophilic proteins is not matched by a substantial increase in their thermodynamic stabilities (on average ~100 kJ/mol) at their physiological working conditions[15]; however, it explains the reduced biological activity of thermostable proteins at moderate temperatures and the requirement of high temperatures for hyperthermophilic organisms to grow.[16] Nevertheless, in protein structures, a topological separation of functional and stabilizing regions in the molecule has been observed[17] and, in rare cases, mutations that increase thermostability, while maintaining low-temperature activity, have been reported.[18,19] The data presently available support the concept that proteins from extremophiles and mesophiles are optimized to maintain corresponding levels of biological activity and structural stabilization at their different working temperatures.[15] Thus, evolutionary adaptation appears to result in the conservation of functionally important intramolecular motions such that, under their optimal physiological conditions, homologous proteins from mesophiles and extremophiles can operate in comparable structural and functional states.[15,20,21]

A number of mesophilic AcP's have been extensively studied in the past few years, leading to a detailed description of the kinetics and thermodynamics of their folding, unfolding, and aggregation processes.[22–27] The kinetic parameters for the reaction catalyzed by AcP's have also been extensively studied.[28,29] The structure of human muscle type and common type AcP (mt-AcP and ct-AcP, respectively), and of an AcP from *Drosophila melanogaster* (Dro2-AcP), have been determined using either NMR spectroscopy or X-ray crystallography.[30–32]

Recently, we have studied in some detail the folding and aggregation processes of an acylphosphatase from Sulpholobus solfataricus (Sso AcP), a hyperthermophilic archaeon growing optimally at 75–85°C and pH 2–4.[33,34] Unlike mt-AcP and ct-AcP, Sso AcP folds from an ensemble of partially folded species that appear rapidly on the submillisecond timescale, and whose formation is believed to be favored by the low net charge, the high hydrophobicity, and the high helical propensity of part of the protein amino acid sequence.[33] In addition, Sso AcP aggregates in the presence of 15–25% trifluoroethanol into protofibrils of amyloid type. Interestingly, the aggregation has been found to occur under conditions in which the protein displays a conformational state that maintains native-like features and enzymatic activity, and whose aggregation is 100-fold faster than unfolding.[34] Such uncommon properties highlight Sso AcP as a model system for folding and aggregation studies worthy of specific attention.

We report here a thorough structural characterization of Sso AcP based on its crystal and solution structures, together with the analysis of its conformational stability and enzymatic activity over a wide range of temperatures. The crystal and solution structures of the enzyme are discussed in light of its thermostability, as well as the kinetics and thermodynamics of its catalytic and folding behavior.

MATERIALS AND METHODS

Cloning, Expression, and Purification of Sso AcP

Sso AcP expression and purification were carried out according to the procedure previously described for the mt- AcP.[35] The resulting sequence was GSMKKWSDTEVFEMLKRMYARVYGLVQGVGFRKFVQIHAIRLGIKGYAKNLPDGSVEVVAEGYEEALSKLLERIKQGPPAAEVEKVDYSFSEYKGEFEDFETY. N-truncated Sso AcP was produced with a mutagenic PCR starting from the wild-type gene inserted in the pGEX-2T plasmid. The amplified fragment was newly ligated into pGEX-2T using the DNA T4-ligase. The resulting plasmid was checked by DNA sequencing and transformed into the DH5-α cells; gene sequence starts from the codon encoding Met11 of the full-length protein. Gene expression and protein purification were carried out as previously described.[35] Protein purity was checked by SDS-PAGE, ES1/MS, and UV absorption; in the latter case, an ϵ_{280} = 0.862 mL mg^{-1} cm^{-1} was used.

Both proteins displayed at the N-terminus the Gly–Ser dipeptide resulting from gene cloning in pGEX-2T. Therefore, in the full length protein the following Met residue is residue no. 1 (with Gly-1 and Ser 0, accordingly). Protein purity and concentration were determined by SDS-PAGE, and ES/MS and UV absorption, respectively; with regard to the latter, an extinction coefficient at 280 nm of 1.246 mL mg^{-1} cm^{-1} was calculated for the full-length protein.

Enzyme Activity Assay

Enzyme activity of Sso AcP was measured by a continuous spectrophotometric method, using benzoylphosphate as a substrate.[36] The main kinetic parameters were determined by measuring the initial rate of benzoylphosphate hydrolysis at pH 5.3 and 25°C (unless otherwise stated) in the presence of substrate concentrations in the 0.2–5.0

m*M* range and in the presence of 0, 1.0, and 2.0 m*M* inorganic phosphate, a known AcP competitive inhibitor. The pH optimum was determined by using 0.1 *M* β,β-dimethylglutarate and Tris-HCl buffers for pH values in the 3.5–7.0 and 7.0–8.0 range, respectively. The temperature dependence of the enzymatic activity was determined by measuring the latter in the standard assay test at temperatures in the 10–55°C range. Due to the chemical instability of the substrate at temperatures higher than 60°C, the enzymatic activity of Sso AcP at the living temperature of the parent organism (75–85°C) could not be measured directly. Therefore, the value of the k_{cat} at 81°C was calculated by extrapolating the temperature-activity data using a polynomial function.

Circular Dichroism

Far- and near-UV CD spectra were acquired at temperatures in the 25–90°C range using a Jasco J-810 spectropolarimeter (Great Dunmow, Essex, UK). Experimental conditions were 0.4 mg mL^{-1} Sso AcP in 5.0 m*M* β,β-dimethylglutarate buffer, pH 6.5 (near-UV). For far- and near-UV CD measurements, 0.1 cm and 1.0 cm quartz cells, both equipped with a stopper to prevent evaporation, were used, respectively.

Dynamic Light Scattering

DLS measurements were carried out on 0.4 mg mL^{-1} Sso AcP dissolved in 5.0 m*M* β,β-dimethylglutarate buffer, pH 6.5, containing 100 m*M* NaCl at temperatures in the 25–82°C range. The data were acquired by using a Zetasizer Nano S DLS device (Malvern Instruments, Malvern, Worcestershire, UK) equipped with a low-volume cell with stopper (path length 3.0 mm, volume 45 μL) and a Peltier thermostatting system.

Conformational Stability

Twenty-six samples, containing 0.2 mg mL^{-1} protein in 50 m*M* acetate buffer, pH 5.5, were equilibrated at one specific temperature in the presence of GdnHCl concentrations ranging from 0 *M* to 6.5 *M*. Far-UV CD spectra were acquired for each sample using the Jasco J-810 spectropolarimeter. The mean residue ellipticity at 222 nm was plotted versus GdnHCl concentration, and the resulting curve was analyzed according to the method by Santoro and Bolen[37] to yield the change of free energy upon unfolding in the absence of denaturant ($\Delta G^{H_2O}_{U\text{-}F}$). The equilibrium curves were acquired at different temperatures (5–85°C), and the resulting plot of $\Delta G^{H_2O}_{U\text{-}F}$ versus temperature was fitted to

$$\Delta G^{H_2O}_{U\text{-}F}(T) = \Delta H_m\left(1 - \frac{T}{T_m}\right) + \Delta C_p\left(T - T_m - T \cdot \ln\frac{T}{T_m}\right), \quad (1)$$

where T_m is the temperature at which the protein is half-denatured, ΔH_m is the enthalpy change upon unfolding at T_m, and ΔC_p is the heat capacity change upon unfolding.

NMR Spectroscopy

^{1}H-NMR spectra were acquired on 0.4 m*M* Sso AcP dissolved in a H_2O/D_2O (90/10) or D_2O containing 50 m*M* sodium phosphate buffer, pH 5.6, and 50 m*M* NaCl. The solution was filtered with a cutoff filter of 0.22 μm, and spectra were collected at 500.13 MHz with a Bruker Avance 500 spectrometer at T = 310 K. 2D TOCSY,[38] DQF-COSY,[39] and NOESY[40] spectra were acquired with solvent suppression obtained by excitation sculpting[41] for H_2O solutions, or presaturation for D_2O solutions, 1–1.5 s steady state recovery time, mixing times (t_m) of 21–56 ms for TOCSY and 100–220 ms for NOESY, t_1 quadrature detection by TPPI,[42] or gradient-assisted coherence selection (echo–antiecho).[43] The spin-lock mixing of the TOCSY experiment was obtained with DIPSI-2[44] pulse trains at $\gamma B_2/2\pi$ = 7–10 kHz. The acquisitions were performed over a spectral width of 7002.801 Hz in both dimensions, with matrix size of 2048 points in t_2 and 256–512 points in t_1, and 96–128 scans/t_1 FID. The set of 2D NMR spectra used to determine the tridimensional structure was acquired within 36 h from sample preparation. Data processing and analysis were performed using Felix (MSI, San Diego, CA) software. All spectra were referenced on Leu62 $H^{\delta 2}$ resonance at 0.529 ppm.

The assignment process of DQF-COSY, TOCSY, and NOESY spectra was performed according to the standard procedure.[45] Internuclear distances were quantified as reported previously[46] from NOESY spectra with t_m = 150 ms using cross-peaks from Gly53 ($H^{\alpha 2}/H^{\alpha 3}$), Tyr94 ($H^{\beta 2}/H^{\beta 3}$) as calibrant. NOESY spectra were further analyzed to identify and quantify correlations related to short-, medium-, and long-range internuclear distances required for restrained modeling.

In addition to internuclear distances, NMR data were also employed to extract the torsion angle ϕ by evaluating $J_{HNH\alpha}$ from H^N-H^α NOESY cross-peak line width at half-height ($\Delta\upsilon^1_2$).[47] This method is considered reliable only if the backbone motional regimen of the protein under investigation is homogeneous, as indeed was the case with Sso AcP. An allowance of ± 30° was introduced for each ϕ angle included in the restraint list. The information on ϕ torsion angles from the fingerprint region of a NOESY spectrum[47] was deliberately limited only to those residues involved in secondary structure motifs to select a subset of backbone atoms that should most likely accomplish the requirement of a homogenous motional regimen. From the analysis of the relative intensities of DQF-COSY, TOCSY, and NOESY H^α-$H^{\beta 2/\beta 3}$ and H^N- $H^{\beta 2/\beta 3}$ cross peaks, it was possible to assign stereospecifically 16 atom or group pairs. The tables of proton assignments and J^3_{HN} values were deposited in the BMRB data bank with accession code 6398.

Structure Generation Procedures

All available experimental information was used as input for restrained dihedral angle MD simulations, performed by using the program CYANA 1.1.[48] In order to use a set of restraints comprising pseudoatoms, two lines to the CYANA code were added to switch to the center-

TABLE I. Structure Quality Parameters for Sso AcP From Restrained Dynamics (CYANA) and Mechanics (DISCOVER) Calculation

Parameter	CYANA	DISCOVER
Number of structures	20	20
Average target function (Å^2)	1.18 ± 0.23 [0.76–1.56]	NA
Average number of violations		
Distance upper limit > 0.2 Å	2.55 ± 3.54 [0–20]	24.15 ± 2.86 [19–29]
Distance lower limit > 0.2 Å	0.30 ± 0.09 [0–3]	7.25 ± 2.07 [3–11]
van der Waals > 0.2 Å	0	ND
Dihedral angles > 5°	0.05 ± 0.00 [0–1]	11.15 ± 2.24 [7–14]
Average maximum violations		
Distance upper limit (Å)	0.36 ± 0.13 [0.20–0.61]	0.43 ± 0.10 [0.34–0.80]
Distance lower limit (Å)	0.17 ± 0.09 [0.05–0.49]	0.68 ± 0.23 [0.42–0.98]
van der Waals (Å)	0.21 ± 0.04 [0.16–0.29]	ND
Dihedral angles (°)	1.58 ± 1.59 [0.26–7.99]	11.23 ± 2.24 [7.69–14.44]
Average violations (/all restr.)		
Distance upper limit (Å)	0.01 ± 0.05	0.02 ± 0.05
Distance lower limit (Å)	0.0 ± 0.01	0.0 ± 0.04
van der Waals (Å)	ND	ND
Dihedral angles (°)	ND	ND
Average sum of violations		
Distance upper limit (Å)	6.60 ± 0.70 [5.00–8.10]	18.73 ± 1.20 [16.74–20.14]
Distance lower limit (Å)	0.80 ± 0.20 [0.40–1.30]	3.72 ± 0.74 [2.26–4.61]
van der Waals (Å)	3.60 ± 0.40 [2.80–4.60]	ND
Dihedral angles (°)	3.50 ± 2.30 [0.90–10.80]	ND
Average RMSD to mean (residues 13–101)		
Backbone (Å)	0.63 ± 0.10	0.64 ± 0.10
Heavy atoms (Å)	1.10 ± 0.11	1.13 ± 0.11
Average energy (/kJ mol^{-1})	$5 \times 10^9 \pm 2 \times 10^9$	$-4.06 \times 10^2 \pm 1.22 \times 10^2$

The experimental set of conformational restraints for torsion angle MD comprised 1019 interatomic distances (d), 386 intraresidue, 289 inter-residue short-range ($d \leq 3$ Å), 116 inter-residue medium range (3 Å $< d <$ 4 Å), 228 inter-residue long-range ($d \geq 4$ Å), 65 dihedral angle restraints, and 16 stereospecific pair assignments.
Minimum and maximum values of the target function, violation numbers, and extents are given in brackets.
NA, not applicable; ND, not determined.

averaging method and treat the distance restraints involving diastereotopic pairs that could not be assigned stereospecifically.

CYANA runs were performed according to the protocol for simulated annealing (8000 steps torsion angle dynamics, 10,000 conjugate gradients minimization steps), with 380 randomly generated starting conformations. The 20 best structures of the CYANA ensemble, in terms of target function, were submitted to restrained minimization using DISCOVER (MSI, San Diego, CA) with the AMBER force field.[49] Overall, the same calculation procedure and parameters were employed as described elsewhere.[50] The analysis of violations and structural parameters of 20 conformers with lower target function obtained from CYANA[48] runs and DISCOVER refinement, summarized in Table I, shows that the distance violation parameters worsen after the refinement process. This is a known effect due to different force fields employed by various modeling programs.[51] The total energy, calculated using AMBER force field within DISCOVER, instead, lowers considerably after refinement. The software packages AQUA and PROCHECK-NMR[52] were used, respectively, to assess the quality of the final structures in relation to the experimental data and to analyze a variety of geometrical parameters that must be fulfilled to match the current validation criteria.[51,52] All structures were visualized and analyzed within the INSIGHTII framework[53] (MSI San Diego, CA) and MOLMOL.[54] The secondary structures of the NMR structural family were evaluated according to the Kabsch and Sander classification.[55] The compactness was calculated according to Zehfus and Rose[56] as the ratio of the solvent-accessible area to the surface area of a sphere with equal volume. The solvent-accessible surface area was evaluated using WHATIF.[57] The solution structure coordinates were deposited in the PDB with the accession code 1Y9O.

Mass Spectrometry

LC-ESI/MS analysis was carried out with a Q-STAR (Applied Biosystems/PE SCIEX), operated in positive elec-

TABLE II. Data Collection and Refinement Statistics

Crystal form	*Triclinic P1*	*Monoclinic P21*
A. Data collection statistics for Sso AcP		
Beamline	ELETTRA XRD-1	ELETTRA XRD-1
λ (Å)	1.200	0.931
Resolution range (Å) (last shell)	30.00–1.27 (1.29–1.27)	29.54–1.90 (1.93–1.90)
Total reflections collected	408,775	132,602
Unique reflections	43,029	25,338
Redundancy	9.5	5.2
Completeness (%) (last shell)	98.9 (98.1)	98.3 (95.7)
*R*merge (%) (last shell)	10.1 (39.5)	8.4 (33.1)
$I/\sigma(I)$ (last shell)	5.2 (3.3)	9.7 (2.9)
Wilson Plot B factor (Å^2)	12.4	26.8
B. Crystallographic refinement statistics		
Unit cell dimension *a,b,c* (Å)	26.19, 36.77, 45.98	48.98, 56.53, 60.81
α, β, γ (°)	81.9, 77.4, 72.4	90.0, 103.7, 90.0
Resolution range used in refinement (Å) (last shell)	8.00–1.27 (1.29–1.27)	8.00–1.90 (1.93–1.90)
R-factor (%)	13.7	16.2
R-free* (%)	17.1	21.5
RMSD bond lengths (Å)	0.012	0.020
RMSD angles (°)	1.227	1.997
RMSD planes (Å)	0.007	0.020
ESU based on max likelihood (Å)	0.050	0.120
Overall mean B factor (Å^2)	15.41	44.37
Ramachandran plot analysis		
Most favored region (%)	91.6	93.2
Allowed regions (%)	8.4	6.8
Disallowed regions (%)	0	0

trospray–ionization mode at atmospheric pressure, and coupled to an Agilent 1100 series micro LC pump equipped with a Phenomenex Jupiter 5μ C18 300 Å (150 × 0,50 mm) column. Chromatographic elution was performed by a 45-min linear gradient from 15% up to 95% of solvent A (0.05% TFA and 0.1% formic acid in H_2O) in solvent B (95% acetonitrile, 5% H_2O, 0.05% TFA and 0.1% formic acid). Typically, the samples of Sso AcP were prepared by diluting an aliquot from NMR solution to micromolar concentration with 0.1% TFA solution or by dissolving directly the lyophilized protein stored at −20°C. Samples were aged by storage in the fridge. A parallel short-term timecourse analysis was carried out on Sso AcP samples prepared from a single mother solution (0.1 m*M*) split into two series; one series was kept in aliquots at room temperature, whereas the other, with individual aliquots in sealed capillaries, was kept in an oven at 90°C, with an overall observation interval of 4 days.

X-Ray Structure Determination

The purified Sso AcP was crystallized as described elsewhere.[58] Diffraction data from two distinct crystal forms (triclinic and monoclinic, respectively) were collected using a synchrotron radiation source (ELETTRA, Trieste, Italy; beamline XRD-1). The experimental diffraction data extend to 1.27 Å and 1.90 Å resolution for the triclinic and the monoclinic crystals (space group $P2_1$), respectively; data collection statistics are reported in Table II(A). The triclinic crystal form displays two Sso AcP molecules per asymmetric unit; four Sso AcP molecules are present in the monoclinic crystals asymmetric unit.[58] The crystal structures of Sso AcP were solved by molecular replacement techniques. After an initial unsuccessful phasing, using the structure of bovine ct-AcP[31] as search model, and different molecular replacement programs,[59–61] a second search model was built, where all Sso AcP nonconserved residues larger than Ala were mutated to Ser (in the bovine ct-AcP model), while keeping the conserved side-chains.

The Sso AcP structure was solved in both crystal forms using the program PHASER.[61] Initial rigid-body refinement of the molecular replacement solutions led to *R*-factor (*R*-free) values of 0.395 (0.415), and 0.377 (0.389), for the P1 and $P2_1$ crystal forms, respectively. Both structures were subsequently refined using the program REFMAC5.[62] Once model building was completed and convergence was reached, solvent molecules were added, following stereochemical rules and difference Fourier maps. Anisotropic B-factor refinement was performed for the triclinic P1 crystal form (final *R*-factor and *R*-free values of 0.137 and 0.171, respectively). TLS refinement was applied to the monoclinic $P2_1$ crystal form (final *R*-factor and *R*-free values of 0.162 and 0.215, respectively; Table II(B)). Atomic coordinates and structure factors of both Sso AcP crystal forms P1 and $P2_1$ have been deposited in the PDB, with accession codes 2BJD and 2BJE, respectively.

RESULTS

Progressive Proteolysis of Sso AcP

Inspection of the 1D and 2D ^{1}H NMR spectra of freshly dissolved Sso AcP (0.4 m*M*) showed slow but appreciable changes over the first 2 to 3 weeks of observation. After several steps of combined NMR and LC-ESI/MS control measurements, this moving target pattern could be safely attributed to a reproducible, progressive proteolytic cleavage at the N-terminal segment of the expressed construct (i.e., the Gly-1 through Ser5 fragment). Additional proteolytic events, involving further cleavage up to Glu11, and hence of the 13 N-terminal residues of the expressed sequence, were observed to occur over periods of several months from sample preparation. Systematic LC-ESI/MS measurements carried out in parallel on Sso AcP samples stored at room temperature and at 90°C showed very similar proteolytic patterns, with different timescales. Mesophilic proteases potentially present as impurities from the expression system or sample manipulation are expected to be inactive at 90°C. In addition, the protease activity was unaffected by the presence, in the sample, of cocktails of protease inhibitors.

A comparable proteolysis was also found to occur during crystal growth. In fact, the electron density maps showed no trace of the N-terminal dodecapeptide (from Gly-1 to Phe10) in both crystal forms. In general, however, any characterization performed on freshly prepared Sso AcP samples (within a few hours from preparation) is not affected, or is influenced only marginally, by proteolysis.

Conformational Stability of Sso AcP at 80°C

The far- and near-UV CD spectra of Sso AcP did not change significantly following a temperature increase from 25°C to 90°C (data not shown). Similarly, DLS measurements showed that the apparent hydrodynamic diameter of the molecule did not change significantly with temperature, with values of 3.85 ± 0.25 and 4.1 ± 0.25 nm at 25°C and 80°C, respectively [Fig. 1(A) and inset therein]. These observations provide direct evidence that the folded conformation of Sso AcP at room temperature does not undergo thermal denaturation or aggregation at the optimal growth temperature of the organism.

The free energy change of Sso AcP unfolding ($\Delta G^{H_2O}_{U\text{-}F}$) was determined at various temperatures by means of equilibrium GdnHCl-induced denaturation curves [Fig. 1(b)]. The plot of $\Delta G^{H_2O}_{U\text{-}F}$ versus temperature, analyzed with Eq. (1), yields values of 4.8 ± 0.9 kJ mol^{-1} K^{-1}, 100.8 ± 4.1°C, 438 ± 44 kJ mol^{-1}, and 20 ± 3°C for the heat capacity change upon unfolding (ΔC_p), the temperature of half-denaturation (T_m), the enthalpy change at T_m (ΔH_m), and the temperature of maximum stability (T_s), respectively (values ± standard deviation). The $\Delta G^{H_2O}_{U\text{-}F}$ value at 28°C is remarkably higher than that of its mesophilic counterparts, both from human and from *D. melanogaster* (Table III), reflecting the need of Sso AcP to work under adverse and destabilizing conditions. At all temperature values, the conformational stability of Sso AcP is higher than that of the previously analyzed mt-AcP[22] and ct-AcP.[25] Nevertheless, Sso AcP and the mesophilic mt-AcP have similar conformational stabilities at the corresponding growth temperatures of the source organisms ($\Delta G^{H_2O}_{U\text{-}F}$ = 20.65 ± 0.3 kJ mol^{-1} at 81°C for Sso AcP and 17.1 ± 0.3 kJ mol^{-1} at 37°C for mt-AcP). Moreover, the difference between the temperature of half-denaturation and the living temperature of the source organism is also similar for the various proteins (Table III). The T_m value of 100.8 ± 1.3°C and the $\Delta G^{H_2O}_{U\text{-}F}$ value of 20.65 ± 0.3 kJ mol^{-1} at 81°C indicate that Sso AcP has a conformational stability sufficiently high to remain folded and functional at the living temperatures of *S. solfataricus*. A mutated form of Sso AcP lacking the first 11 residues displayed a conformational stability very

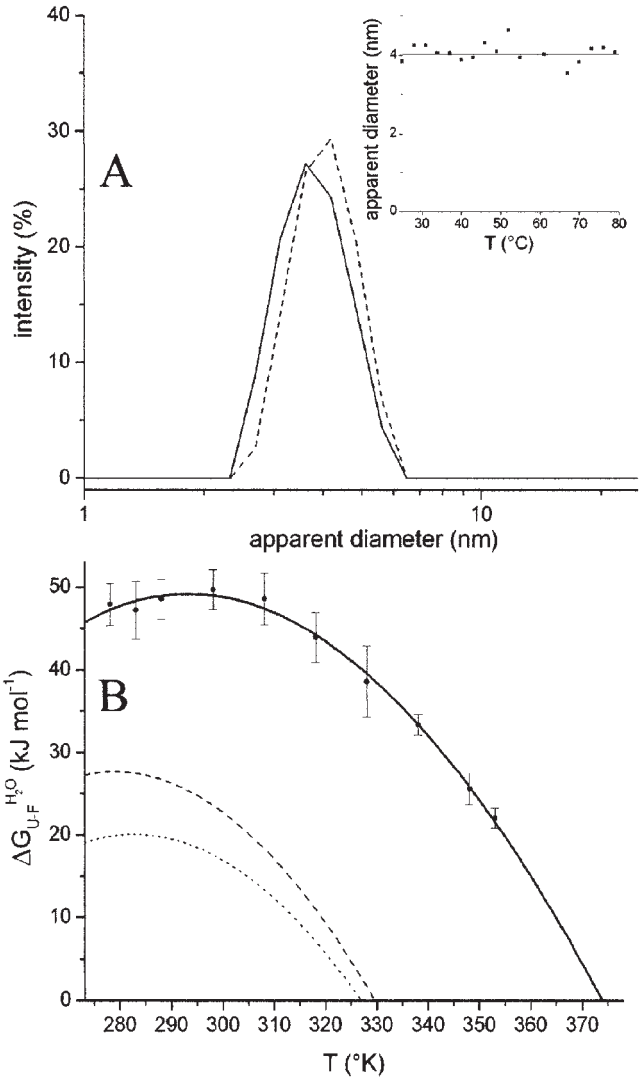

Fig. 1. (**A**) Size distributions of Sso AcP by DLS at 25°C (solid line) and 80°C (dashed line). The analysis yields values of 3.85 ± 0.25 and 4.1 ± 0.25 nm, respectively, indicating that the native protein does not unfold or oligomerize at 80°C. (**B**) Thermal stability curve of Sso AcP (dashed line), mt-AcP (dashed line), and ct-AcP (dotted line). The $\Delta G^{H_2O}_{U\text{-}F}$ data for Sso AcP were obtained by GdnHCl-induced denaturation at various temperatures (see text). The $\Delta G^{H_2O}_{U\text{-}F}$ data for mt- and ct-AcP were obtained previously[22,25] and are shown here for comparison. All measurements were performed in 50 m*M* acetate buffer, pH 5.5. The lines through the data result from the best fit of each set of data to Eq. (1) with the parameters reported in the text and in Table III.

TABLE III. Main Thermodynamic and Catalytic Parameters of Sso AcP in Comparison With Some Mesophilic AcP's[a]

	k_{cat} (s^{-1})	K_M at 25°C (mM)	k_{cat}/K_M at 25°C (s^{-1} mM^{-1})	K_i at 25°C (mM)	Optimum pH	$\Delta G_{U\text{-}F}^{H_2O}$ at 28°C (kJ mol^{-1})	$\Delta G_{U\text{-}F}^{H_2O}$ at 81°C (kJ mol^{-1})	T_m (°C)
mt-AcP	1230 ± 120 (25°C)	0.36 ± 0.04	3400 ± 500	0.75 ± 0.07	4.8–5.8	21.3 ± 2.3	−31.6 ± 0.5	56.55 ± 0.7
ct-AcP	1420 ± 140 (25°C)	0.15 ± 0.02	9500 ± 1400	0.58 ± 0.06	5.0–6.0	16.6 ± 0.3	−30.8 ± 0.4	53.8 ± 0.7
Dro2-AcP	735 ± 75 (25°C)	0.80 ± 0.08	920 ± 140	1.94 ± 0.2	4.8–5.8	13.9 ± 1.3	ND[b]	ND
Sso AcP	198 ± 20 (25°C) 850 ± 85 (81°C)	0.36 ± 0.04	550 ± 80	1.78 ± 0.2	4.7–5.7	48.7 ± 0.7	20.65 ± 0.3	100.8 ± 1.3

[a]The $\Delta G_{U\text{-}F}^{H_2O}$ and T_m values were acquired in 50 mM acetate buffer, pH 5.5. The negative values of $\Delta G_{U\text{-}F}^{H_2O}$ at 81°C for mt-and ct-AcP indicate that these two mesophilic enzymes are unfolded at this temperature. All enzymatic activity measurements were performed in 0.1 M acetate buffer, pH 5.3, using benzoylphosphate and inorganic phosphate as a substrate and competitive inhibitor, respectively. The k_{cat} values from mesophilic AcP's are acquired at room temperature and must be compared with that obtained at 81°C from Sso AcP. Enzymatic activity data for other AcP's have been previously reported.[63] The $\Delta G_{U\text{-}F}^{H_2O}$ values at 28°C for mt-AcP, ct-AcP, and Dro2-AcP are from Taddei et al.,[25] Degl'Innocenti et al.,[29] and Chiti et al.,[63] respectively. The $\Delta G_{U\text{-}F}^{H_2O}$ at 81°C and T_m are from Chiti et al.[22] and Taddei et al.[25] for mt- and ct-AcP, respectively.
[b]ND, not determined.

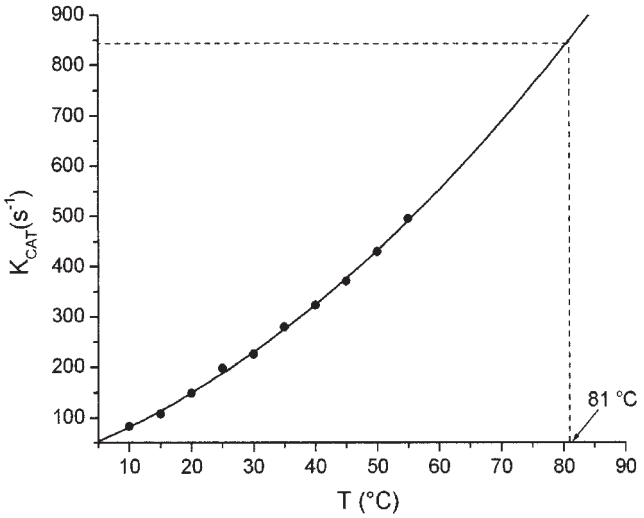

Fig. 2. Enzymatic activity of Sso AcP (k_{cat}) versus temperature. Due to the chemical instability of the substrate, the enzymatic activity of Sso AcP could not be measured directly at temperatures higher than 60°C. The k_{cat} value extrapolated to 80°C using a polynomial function is 850 ± 85 s^{-1}.

similar to that of the full-length protein (unpublished results), indicating that the N-terminal tail is not required for Sso AcP thermostability.

Enzymatic Activity of Sso AcP

The reported catalytic parameters of Sso AcP were determined using the freshly purified full-length protein; the mutant lacking the first 11 residues retains enzymatic activity, indicating that the N-terminal tail is not strictly required for catalysis. Similarly to other AcP's, Sso AcP is able to hydrolyze benzoylphosphate efficiently (Table III). However, note that the enzyme, although displaying pH-optimum, substrate, and inhibitor affinities similar to those of the mesophilic counterparts, is very poorly active at 25°C, as shown by its low k_{cat}. Nevertheless, the latter rises considerably with the temperature (Fig. 2) and at 81°C reaches a value (850 ± 85 s^{-1}, as calculated by extrapolating the temperature-activity data) close to that previously reported for the mesophilic enzymes at 25°C (Table III). The sharp increase of Sso AcP activity with temperature agrees with the widely reported behavior of thermophilic enzymes at high temperatures, where the increased flexibility of the active site is thought to favor the catalytic efficiency.[64]

NMR Analysis

Because of the proteolysis at the N-terminus, a number of extra resonances in the NMR spectra originated from the progressive release in solution of several different peptides. Consequently, the analysis of the NMR spectra of Sso AcP was rather complex (the TOCSY fingerprint is reported in Fig. 3). In particular, the identification of the N-terminal residues of the full-length molecule was seriously affected by the spectral pattern variability leading, for instance, to multiple resonance sets even for expectedly unique spin systems like Trp4. The main difficulty arose from the lack of a definite conformation at the N-terminal segment, which led, for that region, to typical chemical shifts of statistically random polypeptides. By exploiting the slowness of the proteolysis, with NMR spectra recorded within 36 h from sample preparation, we were able to observe all residues of the full-length protein but the N-terminal tripeptide Gly-1-Ser0-Met1.

The main indicators of the structure quality survey by AQUA and PROCHECK-NMR[52] are reported in Table IV, together with the corresponding consensus values. It is clear that the conformational family of Sso Acp in solution matches the accepted criteria for structure validation.

Structure of Sso AcP

Similarly to other structurally determined AcP's, Sso AcP displays an α/β sandwich domain composed of four antiparallel and one parallel β-strands, assembled in a five-stranded, twisted β-sheet facing two antiparallel α-helices; the sheet arrangement follows the 4-1-3-2-5 β-strand topology found in known AcP structures.[30–32] By analogy with other AcP structures, the six loops connecting the secondary structure elements have been labeled L1 through L6, starting from the N-terminus.

Structural alignment of AcP's from mesophilic and hyperthermophilic organisms shows that Sso AcP has an

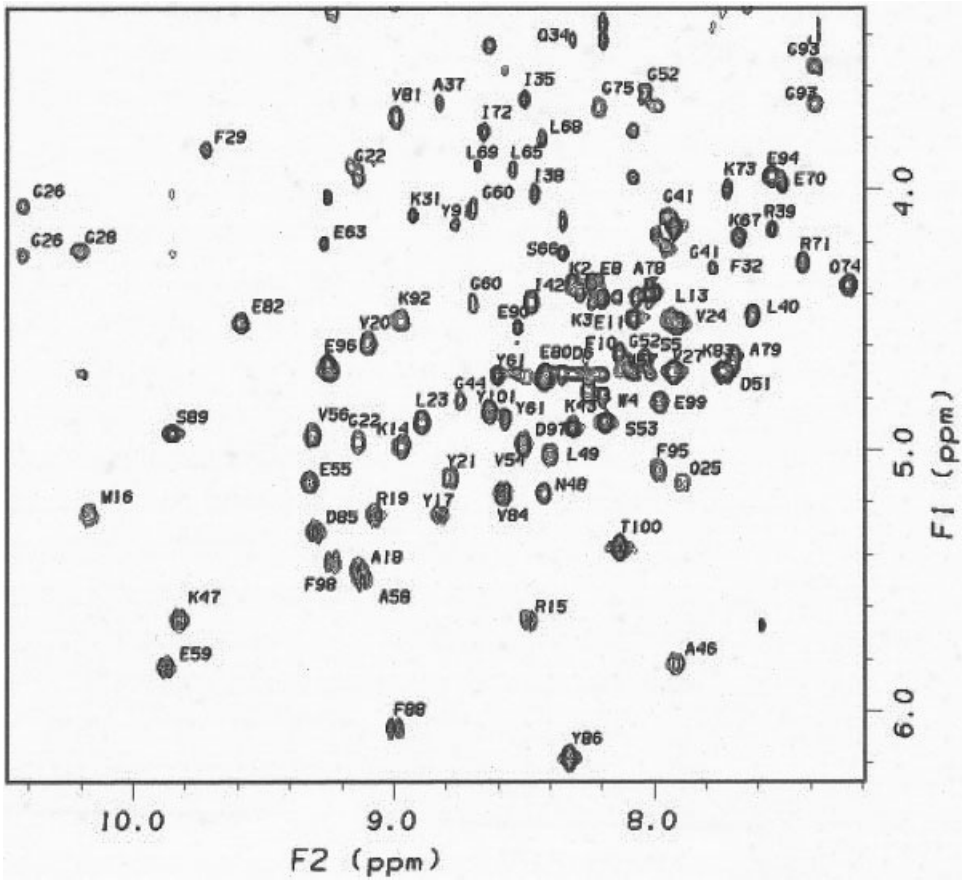

Fig. 3. Fingerprint region from 500 MHz ^{1}H 2D TOCSY spectrum of 0.4 m*M* Sso AcP in 50 m*M* phosphate buffer, 50 m*M* NaCl, at pH 5.6, $T = 310$ K. The H^N–H^α connectivity assignments are indicated by amino acid single-letter code.

additional segment at the N-terminus with respect to the other proteins considered (Fig. 4). In agreement with the alignment, the structured part of Sso AcP begins at residue 13, whereas the preceding tail is almost completely devoid of any defined conformation, as shown in Figure 5(A). Indeed the inspection of the NMR experimental restraint set reveals the absence of medium- or long-range constraints in the first 14 residues except for Met12 (i.e., the residue that precedes the start of strand S1).

The 20 best solution conformers have an RMSD from their mean structure, calculated on residue range 13–101, of 0.64 Å and 1.13 Å for backbone and non-hydrogen atoms, respectively. These values indicate that the spread within the conformer family is, on average, very limited. A conformational spread larger than mean values is present in the loop regions: in particular, loops L1 and L3, connecting strand S1 and helix H1, and strands S2 and S3, respectively, are more disperse than average, with a backbone RMSD of 0.9 Å. Conversely, loops L2 and L4, connecting H1 and S2, and S3 and H2, respectively, are short, and their dispersion is comparable with that of the entire molecule. Loop L5 joins helix H2 to strand S4, with a backbone RMSD of 0.8 Å, whereas L6, which is 9 residues long and connects strands S4 and S5, spreading from one edge of the sheet to the opposite, shows an average backbone RMSD value of 0.7 Å. This reduced dispersion is consistent with a more rigid loop, which is strengthened by the salt bridge between Glu87 and Lys36.

In both Sso AcP models refined for the triclinic and monoclinic crystal forms, respectively, all residues built lie within the allowed regions of the Ramachandran plot. In the P1 case, the refined model is well defined for residues Glu11 through the C-terminus Tyr101, with ideal stereochemical parameters, for both molecules present in the asymmetric unit. Similarly, the Sso AcP structure is well defined in the Glu11–Tyr101 range for the four independent molecules of the $P2_1$ crystal form [Table II(B)]. Structural superpositions [Fig. 5(B)] between the six independent copies of the Sso AcP molecule here reported indicate a strong structural conservation, despite different crystal packing modes. RMSDs calculated for the six models, over the 11-101 residue range (on 91 Cα pairs), range in the 0.35–0.50 Å interval, with a mean value of 0.41 Å. Overall, the Sso AcP molecule occupies a volume of about 34 Å × 22 Å × 19 Å, appearing slightly more compact relative to the AcP structures reported so far, in relation to a shorter L6 loop (8 residues in Sso AcP vs 10 residues in ct-AcP; Fig. 4). Accordingly, the hydrodynamic diameter, as calculated by pulse field gradient NMR,[65] gave values of 3.5 ± 1.2 nm for Sso AcP (the core enzyme

TABLE IV. Structure Validation Parameters for Sso AcP Conformers from NMR Data Refinement (DISCOVER)

Parameter	This work	Consensus standard[a]
Total residues/selected residues[b]	103/74	74 ± 39/62 ± 36
Number of conformers	20	20 ± 15
Restraints per residue[c,d]	11.1	11.3 ± 4.5
NOE root-mean-square violation (Å)[e]	0.056	0.061 ± 0.043
Ramachandran quality[b] (%)		
Residues in most favored regions	75.4	73.6 ± 15.5
Residues in additional allowed regions	24.1	NA
Residues in generously allowed regions	0.4	NA
Residues in disallowed regions	0.1	NA
Average G-factors[b,f]		
ϕ–ψ	−0.86	NA
χ^1–χ^2	−0.95	NA
χ^1 only	−0.42	NA
Overall	−0.85	NA

NA, not available.
[a]From Doreleijers et al.[51]
[b]According to Doreleijers et al.,[51] the listed parameters, except for the NOE rms violation, were calculated on well-defined segments of the protein; namely, only those residues for which the average of the circular variance of the backbone angles ϕ and ψ was < 0.2 were included in the selected segments.
[c]To avoid the redundancy of considering upper and lower bounds, only a single distance bound per internuclear separation was included in the count. Thus, 1019 NOE and 65 dihedral angle restraints were included in the count.
[d]Referred to the reduced NOE-restraint set above considered from well-defined segments.
[e]Referred to all residues.
[f]Low *G*-factors indicate low-probability conformations.[52] As a rule of thumb, acceptable overall values range around −1.

without the N-extension and 3.6 ± 1.2 nm for both ct- and mt-AcP's. Such a structural feature results in an increased number of intramolecular interactions contributing to the stabilization of the N-terminal β-strand (S1), and in the complete absence of protein core cavities.

The analysis of packing modes shows that Sso AcP intermolecular contacts are entirely different in the two crystal forms. The two asymmetric unit molecules of the triclinic crystal form make contacts at the L3 loops of both partners and at strands S1 and S4 of one molecule to the L4 loop of the other. A Cd^{2+} cation from the crystallization medium bridges the two molecules by electrostatically coupling residues Asp78 of both chains. The effects of crystal packing appear very reduced, with the RMSD calculated over 91 Cα pairs for the two Sso AcP molecules being 0.43 Å; the largest structural deviations (0.5 Å) are located at the L3 and L4 loops. In the monoclinic crystal form, the four independent molecules display several contacts scattered over the molecular surfaces. Regions involved in contacts include the S2, S4, and S5 strands, the L1, L3, and L5 loops, and the H1 and H2 helices. However, in all cases the intermolecular packing surfaces are of limited size, mostly mediated by intervening water molecules and not indicative of Sso AcP quaternary structure association trends. Inspection of the crystal packing regions, after optimal overlay of the four independent models (mean RMSD of 0.44 Å), shows that the largest backbone conformational deviations (potentially ascribable to crystal packing contacts) are located at the L5 loop (residue Pro76, maximum Cα deviation of 1.7 Å), at the L6 loop (residue Glu94, maximum Cα deviation of 1.1 Å), and at the L3 loop (residue Pro50, maximum Cα deviation of 0.9 Å).

Although the solution and crystal structures were solved on Sso AcP molecules differing for the presence–absence of the first 12 residues, respectively, the two approaches yield quite comparable results. Moreover, the ^{1}H chemical shifts of the various residues in the AcP domain did not change during the progressive cleavage of the N-terminal region, indicating that the N-terminal fragment is not required to maintain the observed AcP fold in the extremophilic enzyme.

Besides the absence of the N-terminal segment (Fig. 5), other relevant differences between the crystal and solution structure involve loops and helix H2. L4, a short, two-residue loop, is absent in the crystallographic structure, where strand S3 and helix H2 are directly connected. Overall, the RMSD between the mean solution structure and the mean crystal structure is 1.8 Å and 2.6 Å for backbone and all non-hydrogen atoms, respectively. The main difference involves helix H2, which is bent toward the exterior by 12° in the NMR conformation relative to the X-ray structure, with consequent enlargement of the cleft between helix H2 and the facing sheet. This displacement does not appear to be related to the N-terminal tail present in the solution structure. The following L5 loop is wider in the solution structure, where it appears as a tight hairpin. When observed from the side opposite the N-terminus, the two Sso AcP loops (L1 and L5) connecting the helices to the sheet are both similarly shifted toward L3 in the NMR mean structure relative to the X-ray conformation, thus running almost parallel in both structures. No similar

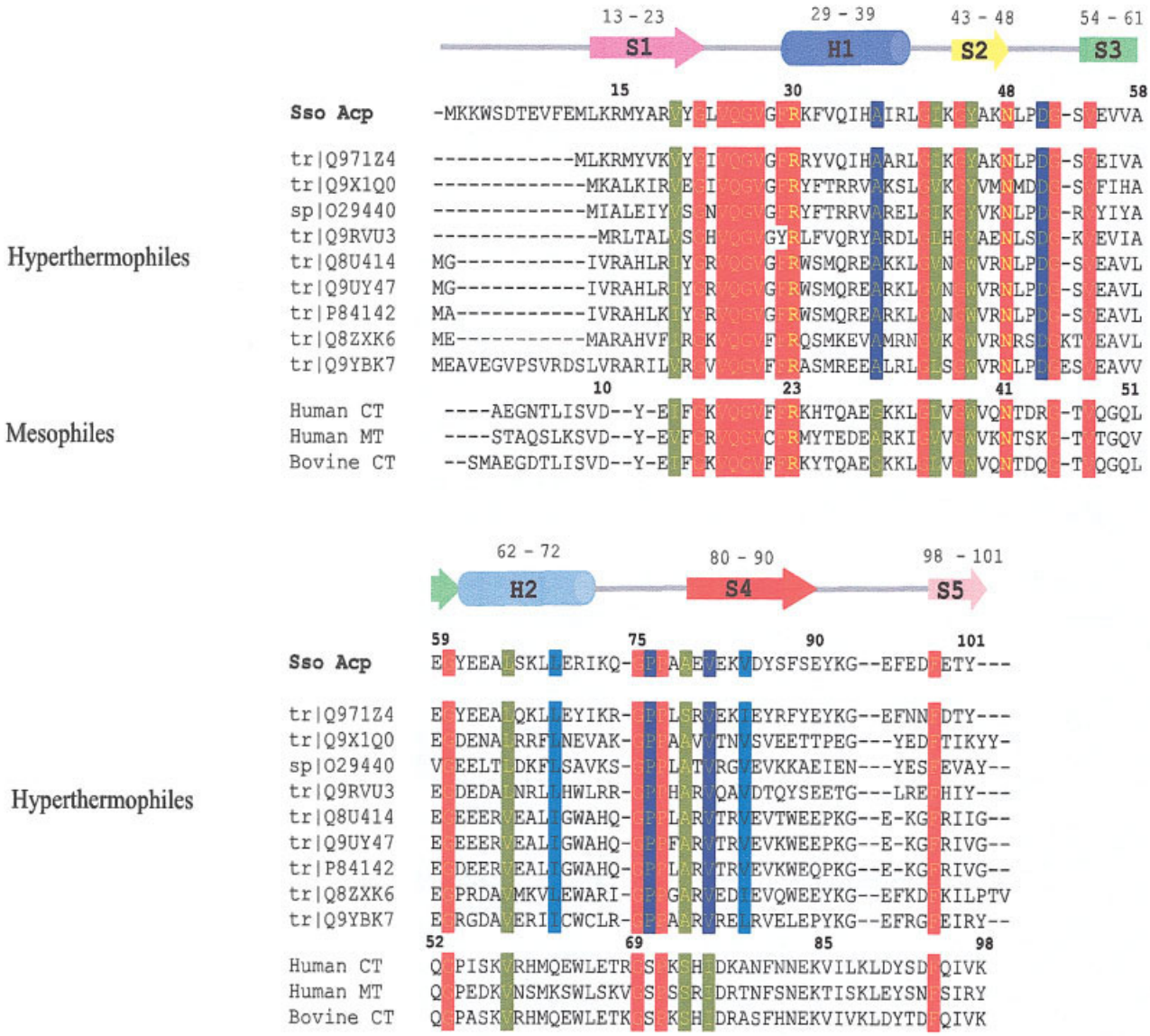

Fig. 4. Structure-based sequence alignment of selected AcP's from extremophiles and from mesophilic sources. The amino acid numbering scheme adopted for Sso AcP is shown on the top line; the conventional mesophilic AcP sequence numbering is shown on top of the human ct-AcP. Red and green bars indicate residues that are conserved or conservatively replaced among all phyla, respectively. Blue and cyan bars refer to residues conserved, or conservatively substituted, among extremophilic AcP's (Q971Z4 *Sulfolobus tokodaii*; Q9X1Q0 *Thermotoga maritima*; O29440 *Archeoglobus fulgidus*; Q9RVU3 *Deinococcus radiodurans*; Q8U414 *Pyrococcus furiosus*; Q9UY47 *Pyrococcus abyssi*; P84142 *Pyrococcus horikoshii*; Q8ZXK6 *Pyrobaculum aerophilum*; and Q9YBK7 *Aeropyrum pernix*). The secondary structure elements of Sso AcP crystal structure, reported on the top of the figure, are numbered according to the previously mentioned scheme.

shift occurs at loop L3 in the mean NMR geometry; therefore, the cradle that embeds the active site, between helix H1 and strand S2, appears deeper in the crystal than in the solution structures.

Analysis of Salt Bridges and Hydrogen Bonds

Unlike the known mesophilic AcP's, the Sso AcP protein surface is characterized by 7 Tyr residues and by 22 charged residues, which may support salt bridges and/or hydrogen bonded interactions. As far as the total number of hydrogen bonds and of side-chain–side-chain hydrogen bonds is concerned, it does not vary significantly among the different hyperthermophilic and mesophilic species. Instead, two main clusters involving charged residues can be recognized on the solvent face of the five-stranded β-sheet (Fig. 6). The first one involves residues Lys14, Arg15, Glu59, Glu62, and Glu94; the second includes residues Tyr17, Arg19, Tyr45, Lys47, Asp51, and Glu55. In the first cluster, Arg15 is electrostatically coupled to Glu59 and, in the crystal structures, is also hydrogen bonded to Glu94, thus anchoring the S1 strand to the protein core and stabilizing the L6 loop. Such a bipartite salt bridge cannot occur in bovine ct-AcP, where residue 8 (corresponding to Arg15) is Ser. In the crystals, residue

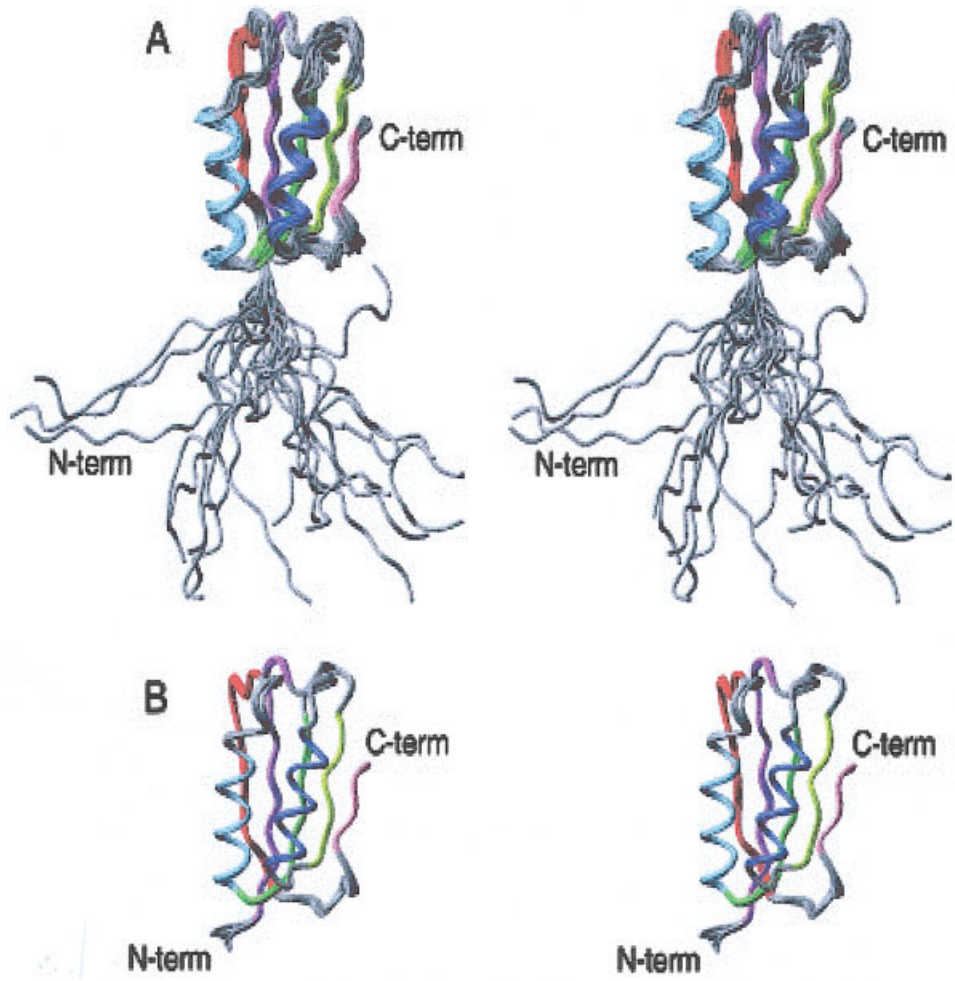

Fig. 5. Overview of the best-fit superimposition of (**A**) the 20 final conformers of Sso AcP after DISCOVER refinement (MSI) of the NMR-restrained ensemble obtained from CYANA[48] and of (B) the six independent molecules resolved by X-ray crystallography. The fitting was obtained superimposing Cα atoms of all residues and of residue range 11–101 for the X-ray and NMR ensemble, respectively. The backbone RMSDs of residues 1–11 and 12–101 of the 20 NMR structures with respect to mean structure are 13.0 Å and 0.63 Å, respectively. The RMSDs of the six independent X-ray conformers, as calculated over pairs of Cα backbones, are all less than 0.52 Å (0.42 Å on average). Only backbone atoms are drawn. The secondary structure elements are drawn according to the following color code:

S1, H1, S2, S3, H2, S4, S5.

Glu59 (replaced by Gln52 in the bovine ct-AcP) is involved in two additional interactions, with the peptidic N atoms of residues Lys92 and Glu94. In solution, Lys43 is consistently salt-bridged over the NMR family to Glu59 (thus connecting strand S2 to S3) and to Glu94 (thus connecting strand S2 to the loop L6, hence stabilizing the latter).

The second cluster, with the exception of Asp53, contains residues belonging to different β-strands; it may be involved in the stabilization of the five-stranded β-sheet region harboring the catalytic Asn48 residue (corresponding to Asn41 in mt- and ct-AcP's), and in structural support to the extended L3 loop through Asp51. Isolated ion pairs are formed by residues Glu63–Ly67 and Glu70–Arg71, in the second α-helix (H2) on the opposite face of the Sso AcP molecule. The L5 loop, instead, is stabilized by hydrophobic contacts to the protein core.

The active site residue Arg30 (corresponding to Arg23 in mt- and ct-AcP's) is salt-bridged to the C-terminal carboxylate of Tyr101. This salt bridge has the double effect of anchoring the C-terminal S5 strand to the protein core and blocking Arg30 in a firmly defined conformation, thus stabilizing the active site region by limiting Arg30 flexibility. Phe98 (which is conserved in the thermophilic AcP's) plays a similar role by participating in a hydrophobic cluster anchoring S5 to the protein core (a complete list of H-bonds and salt bridges is reported in Tables S1 and S2 of Supplementary Material).

Residue Conservation in Hyperthermophilic AcP's

The analysis of amino acid sequence alignments of AcP's from thermophilic and mesophilic sources (Fig. 4) highlights a series of residues that appear to be specifically

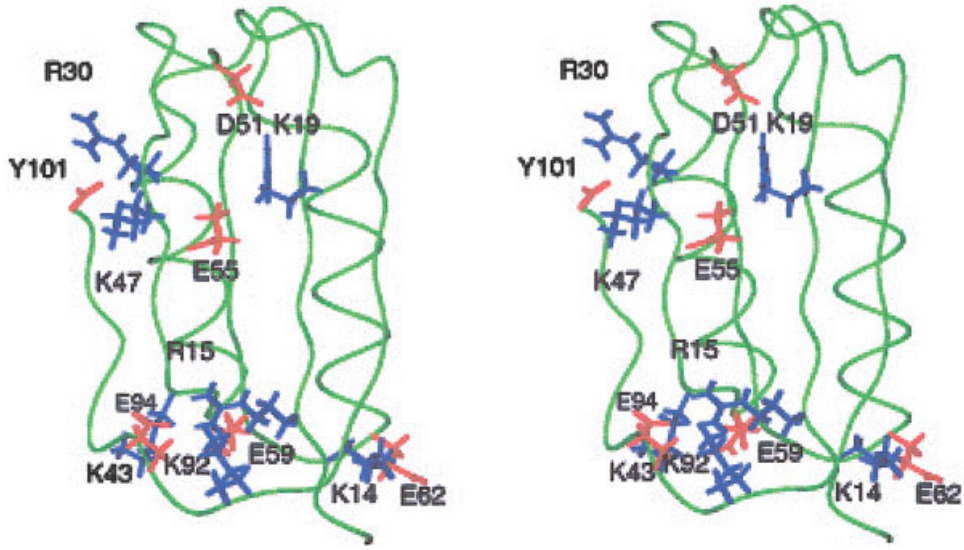

Fig. 6. A stereoview of the electrostatic network. In red and blue are highlighted negatively and positively charged residues, respectively.

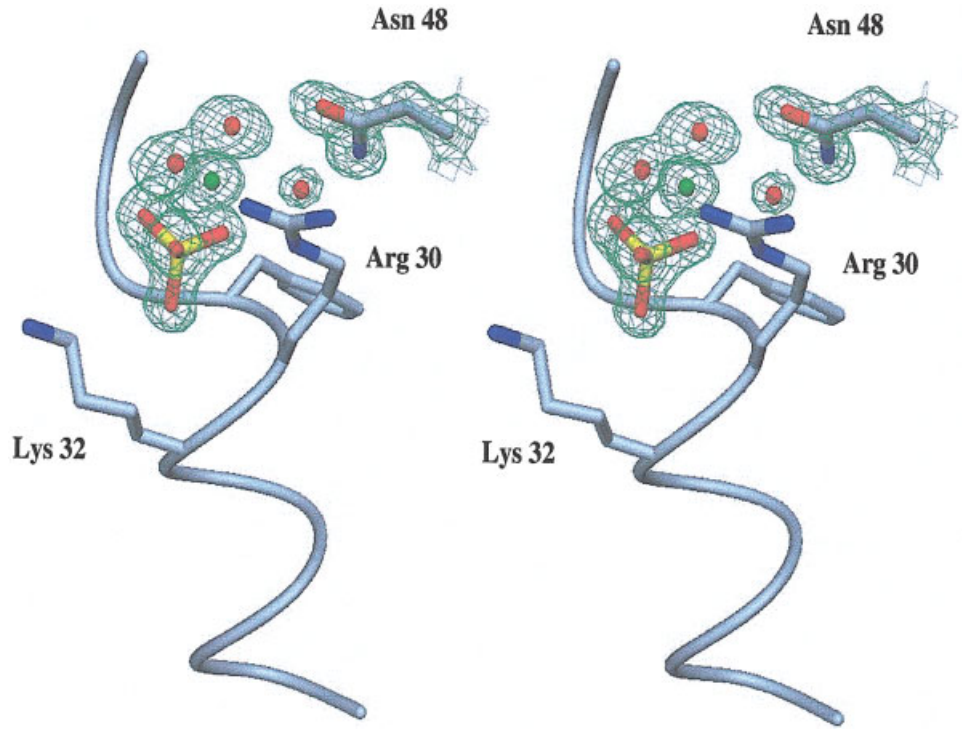

Fig. 7. A stereoview of the Sso AcP active site region with the bound sulfate anion, as observed in the 1.27 Å resolution triclinic crystal structure, together with the observed electron density (asymmetric unit molecule B). The catalytic key residues Arg30 and Asn48 are shown for reference; the α-helical region shown is from helix H1. The electron density is contoured at 1.0 σ-level.

conserved in the thermostable AcP's. In the N-terminal region, the S1 strand sequence is highly variable among species. However, the L1 loop sequence, housing residues involved in substrate recognition and binding, is highly conserved among all the phyla, displaying the most stringent AcP sequence fingerprint (see below). The H1 helix hosts at its N-terminus the conserved Arg30 (corresponding in mt- and ct-AcP's to Arg23, one of the two residues involved in catalysis).[66,67] The L2 loop displays the conserved sequence motif Gly-Ile/Leu/Val-X-Gly, where X is a polar residue, in hyperthermophilic bacteria. Asn48 (corresponding to Asn41, the second recognized catalytic residue in mt- and ct-AcP's)[67] is the only significantly conserved residue in the S2 strand. The L3 loop displays a conserved

Asp51 in hyperthermophilic AcP's, while Gly52 is conserved in all species. Gly60 in the L4 loop is also common to all AcP's. The H2 helix harbors two hydrophobic residues at positions 61 and 62 in hyperthermophilic AcP's, whereas residue 62 is mainly polar in the mesophilic counterparts. The L5 loop displays the Gly-Pro-Pro-X-Ala-X-Val motif conserved only in the hyperthermophilic and *Deinococcus radiodurans* AcP's. The presence of two Pro residues may confer specific structure and/or structural rigidity to this loop which is not stabilized by intramolecular ion pairs. No other conserved residues are observed in the S4 strand nor in the L6 loop; the latter in Sso AcP is two residues shorter than in the bovine ct-AcP. Phe98 in strand S5 is conserved in hyperthermophilic AcP's, most likely in relation to β-sheet stabilization through hydrophobic contacts.

Substrate-Binding Site

In Sso AcP, the sequence of the universally conserved AcP signature (Val-Gln-Gly-Val-X-X-Arg, residues 24–30 corresponding to residues 17–23 in mt- and ct-AcP's) defines a cradlelike conformation of the polypeptide backbone; the latter, on the basis of homologous AcP structures[30–32,68] and of site-directed mutagenesis studies[66,67] can be identified as the substrate-binding site. The Sso AcP structure in the monoclinic crystal form (refined at 1.90 Å resolution) shows a tightly bound tetrahedral species in the active site cradle, recognized as a sulfate anion in the electron density maps of each of the four independent molecules. The sulfate anion, provided by the lithium sulfate crystallization agent, is neighbored by two water molecules and directly hydrogen-bonded to the backbone N atoms of residues Gly28, Arg30, Lys31, and to the NE2 atom of Arg30. Furthermore, the sulfate anion is bridged through a structured water molecule to the Asn48 OD1 atom. By analogy with ct-AcP, such a water molecule, activated by hydrogen bonding, is likely to act as the nucleophile in the catalytic mechanism of AcP hydrolysis when the proper substrate is bound.[69]

A different behavior for the active site region of the two independent molecules is observed in the triclinic Sso AcP crystal form (refined at 1.27 Å resolution). While molecule B clearly displays the active site bound sulfate moiety, together with three structured water molecules (Fig. 7), the electron density of the liganded anion is more disturbed in molecule A. Refinement of atomic occupancies suggests that the presence of the sulfate (at 30% occupancy) is competed by two Cl^- ions (known AcP competitive inhibitors; 70% occupancy) and by water molecules. The presence of two Cl^- anions ensures electrostatic balance of the active site positive charges mainly provided by residues Arg30 and Lys31.[70]

In solution, the active site cavity appears, in about 50% of the conformers, not as deep as in the crystal, and the long side-chains of Lys31 and Arg30 provide two closely spaced, positive regions delimiting the active site pocket. The differing depth of the cradle may be due to the presence of different anions bound to the active site, namely, phosphate and sulfate in NMR and crystallographic experiments, respectively. It is worth noting that in solution, the sample is buffered with phosphate, known to be a good AcP competitive inhibitor; therefore, in our experimental conditions, it will be bound to the substrate-binding site. The previously determined NMR structure of the horse muscle AcP[30] at 37°C, when compared to the NMR conformers of Sso AcP, displays much higher global RMSDs of the ensemble and, in particular, highly dispersed loop regions. Loop L3, which is close to the active site, exhibits backbone RMSDs of 0.9 Å and 2.3 Å relative to the corresponding mean structures for the Sso and horse muscle AcP, respectively.

DISCUSSION

We have determined the crystal and solution structures, together with the main parameters describing the enzymatic activity and conformational stability of the AcP from the hyperthermophile archaeon *S. solfataricus*. Such an integrated approach has allowed us to compare the protein structure in different environments, also focusing on the structural adaptations underlying Sso AcP thermostability.

An unexpected, possibly proteolytic activity was observed in the protein, resulting in the progressive loss of the unstructured, mobile N-terminal segment. Such a proteolysis, detected at high protein concentrations and apparent over long timescales, does not affect the conformational stability of the protein nor abolish enzymatic activity. The catalytic and stability properties of Sso AcP are comparable to those of mesophilic AcP's, under their respective working conditions (80°C and 37°C, respectively). These observations support the notion that corresponding mesophilic and extremophilic proteins are in comparable functional states, and display similar structural stabilities and catalytic efficiencies when tested under conditions reflecting those required for optimal growth of their biological sources.[15,20,21]

Insights on the Active Site of Sso AcP

Sso AcP displays poor catalytic efficiency at 25°C; this observation may be related to the enzyme molecular rigidity. In fact, comparing the NMR conformational ensemble of the mesophilic mt-AcP[30] to our data on Sso AcP recorded at the same temperature, a much higher dispersion of the former ensemble with respect to the latter is apparent. This holds true particularly for loop L3, which is close to the active site. In fact, the RMSD of a region, averaged over a family of conformers, can be related to the atomic mobility, especially for small, single-domain globular proteins.

As far as the active site is concerned, the presence of a strong salt bridge in Sso AcP (not present in ct-AcP) between Arg30 (Arg23 in ct-AcP) and the C-terminus carboxylate may stiffen the catalytic site region, thus reducing enzyme activity. The latter does not appear to result from a reduced accessibility of the substrate-binding region due to the presence of the salt bridge; in fact, at 25°C, the affinities of Sso AcP for both the substrate and the competitive inhibitor inorganic phosphate are very similar to those previously reported for other mesophilic

AcP's where such a bridge is not present. Rather, it appears to stabilize the substrate-free active site similarly to the substrate itself.[71] At the enzyme working temperature of about 80°C, the increased kinetic energy can overcome the detected rigidity of the active site and of neighboring regions, resulting in enzyme activity comparable to that displayed by the mesophilic counterparts at 25°C.

The Sso AcP crystal structures were determined at 100 K; therefore, analysis of their atomic temperature B-factors in relation to protein flexibility may bear only a qualitative value. However, two main issues in such analysis may be worthy of comment. First, the B-factor profiles of Sso AcP match qualitatively those observed in the crystal structure of Dro-2-AcP, also determined at 100 K.[29] For both proteins, the correlation between low B-factors and secondary structure elements is evident, with loops displaying the maxima, and helices and strands, the minima. However, the average main-chain B-factors differ by about 10 $Å^2$, being higher for the mesophilic protein. In addition, the B-factor profiles of both proteins show that the two catalytic residues Arg30 (Arg23 in Dro2-AcP) and Asn48 (Asn41 in Dro2-AcP) fall in regions of generally low B-factors, although not in the absolute minimum.

The N-Terminal Segment

The solution structure of Sso AcP determined by NMR spectroscopy displays the entire protein and clearly shows a high degree of freedom for the unstructured 11-residue N-terminal region. The presence or the absence of the N-terminal fragment does not appear to affect the well-known AcP fold, as is evident from the comparison of the NMR and crystallographic data obtained on the full-length and truncated protein, respectively. However, analysis of the Sso AcP unstructured N-terminal tail, which might be considered an extra fragment bound to the AcP fold at Met12, raises two particularly interesting observations. First, it allowed the detection of a possible weak and unexpected protease activity for Sso AcP. To our knowledge, such an activity has never been reported previously for any AcP, despite shorter and unstructured N-terminal segments are present in other members of the family (Fig. 4). Quantitative kinetics assessments of the hypothesized proteolytic activity of Sso AcP are currently under way to address the issue.

The second important aspect, related to the unstructured Sso AcP N-terminal tail, is its involvement in the uncommon protein aggregation behavior starting from a nativelike conformation in the presence of 15–25% trifluroethanol.[34] The propensity toward aggregation of a nativelike conformation is a rather peculiar behavior among AcP's and can be explained by the unstructured N-terminal tail acting as a nucleation element favoring the initial assembly of the monomers while these still retain a nativelike conformation. Experiments are now in progress to ascertain the importance of the N-terminal segment in favoring Sso AcP aggregation.

Structural Factors Enhancing Stability

Thermodynamic evidence indicates that Sso AcP is very stable at room temperature, as compared to its mesophilic homologs. The proposed factors that influence thermostability in hyperthermophilic proteins are surface loop deletion/shortening, increased packing efficiency, increased propensity to form α-helical structure within regions of the sequence that adopt an α-helical conformation, and increased number of salt bridges and hydrogen bonds between side-chains.[2–8]

In Sso AcP, a comparative analysis of the amino acid sequences shows that the ratio between charged and uncharged polar residues is about 1 for Sso AcP and drops to 0.6 for ct-AcP and 0.65 for mt-AcP, in agreement with other hyperthermophilic AcP's. Our structural analysis indicates that the number of hydrogen bonds between the side-chains is constant in the various AcP's, ruling out an involvement of this factor in the higher stability of Sso AcP. Instead, at the surface of Sso AcP, a higher number (14) of salt bridges is present than that found in ct-AcP (10 salt bridges). In addition, in Sso AcP, the salt bridges appear to form a regular network of electrostatic interactions further stabilizing the β-sheet. The C-terminal region, already recognized as a key region in molecular stabilization of mt-AcP,[72] is strengthened in hyperthermophilic AcP's by the presence of a tight salt bridge between the C-terminus and the catalytic Arg30 residue. Moreover, the presence of three salt bridges in the L6 loop of Sso AcP and, similarly, of the AcP from *P. horikoshii*, may be crucial for the stabilization of that region.[68] Furthermore, unlike the other loops, this loop is also two residues shorter in the two hyperthermophilic AcP's than in the mt- and ct-AcP.

As far as the intrinsic stability of the α-helices is concerned, the amino acid sequence corresponding to the first α-helix of Sso AcP displays a low α-helical intrinsic propensity, as assessed by AGADIR,[73] although this program is best suited to predict helix propensity of the amino acid sequences in isolation rather than in compactly folded proteins. However, the sequence corresponding to the second helix (residues 56–67 and 55–65, according to the NMR and crystal structures, respectively) has a helical propensity over 10-fold higher than those of the corresponding sequences of mt- and ct-AcP. This increased propensity may contribute to the high conformational stability measured for the overall fold of Sso AcP.

Another important determinant of protein thermostability is the protein density packing.[2,7] We have calculated according to method of Zehfus and Rose[56] the protein compactness (see Materials and Methods section): lower values are indicative of tighter packing. The resulting values were lower for Sso Acp (2.2) with respect to ct-AcP (2.4) and mt-AcP (2.4), indicating that the hyperthermophilic protein is more densely packed than the mesophilic counterparts. In summary, the structural factors enhancing Sso AcP stability are the presence of an ion-pair network at the protein surface, the presence of specific salt bridges in strategic positions, the higher α-helix propensity in helix-2, and a more tight overall packing density.

REFERENCES

1. Lo Leggio L, Kalogiannis S, Bhat MK, Pickersgill RW. High resolution structure and sequence of *T. aurantiacus* xylanase I: implications for the evolution of thermostability in family 10 xylanases and enzymes with (beta)-alpha-barrel architecture. Proteins 1999;36:295–306.
2. Thompson MJ, Eisenberg D. Transproteomic evidence of a loop-deletion mechanism for enhancing protein thermostability. J Mol Biol 1999;290:595–604.
3. Karshikoff A, Ladenstein R. Ion pairs and the thermotolerance of proteins from hyperthermophiles: a "traffic rule" for hot roads. Trends Biochem Sci 2001;26:550–556.
4. Pace N. Single surface stabilizer. Nat Struct Biol 2000;7:345–346.
5. Perl D, Mueller U, Heinemann U, Schmid FX. Two exposed amino acid residues confer thermostability on a cold shock protein. Nat Struct Biol 2000;7:380–383.
6. Pace N, Alston RW, Shaw KL. Charge–charge interactions influence the denatured state ensemble and contribute to protein stability. Protein Sci 2000;9:1395–1398.
7. Szilagyi A, Zavodszky P. Structural differences between mesophilic, moderately thermophilic and extremely thermophilic protein subunits: results of a comprehensive survey. Struct Fold Des 2000;8:493–504.
8. Cambillau C, Claverie JM. Structure and genomic correlates of hyperthermostability. J Biol Chem 2000;275:32383–32386.
9. Kumar S, Tsai CJ, Nussinov R. Thermodynamics differences among homologous thermophilic and mesophilic proteins. Biochemistry 2001;40:14152–14165.
10. López-Hernández E, Cronet P, Serrano L, Muñoz V. Folding kinetics of Che Y mutants with enhanced native alpha-helix propensities. J Mol Biol 1997;266:610–620.
11. Deckert G, Warren PV, Gaasterland T, Young WG, Lenox AL, Graham DE, Overbeek R, Snead MA, Keller M, Aujay M, Huber R, Feldman RA, Short JM, Olsen GJ, Swanson RV. The complete genome of the hyperthermophilic bacterium *Aquifex aeolicus*. Nature 1998;392:353–358.
12. Scheraga HA. Theory of hydrophobic interactions. J Biomol Struct Dyn 1998;16:447–460.
13. Tekaia F, Lazcano A, Dujon B. The genomic tree as revealed from whole proteome comparison. Genome Res 1999;9:550–557.
14. Choi IG, Kim SS, Ryu JR, Han YS, Bang WG, Kim SH, Yu YG. Random sequence analysis of genomic DNA of a hyperthermophile: *Aquifex pyrophilus*. Extremophiles 1997;1:125–134.
15. Jaenicke R. Protein stability and molecular adaptation to extreme conditions. Eur J Biochem 1991;202:715–728.
16. Jaenicke R, Böhm G. The stability of proteins in extreme environments. Curr Opin Struct Biol 1998;8:738–748.
17. Shoichet BK, Baase WA, Kuroki R, Matthews BW. A relationship between protein stability and protein function. Proc Natl Acad Sci USA 1995;92:452–456.
18. van den Burg B, Vriend G, Veltman OR, Venema G & Eijsink VGH. Engineering an enzyme to resist boiling. Proc Natl Acad Sci USA 1998;95:2056–2060.
19. Giver I, Gershenson A, Freskgard PO, Arnold FH. Directed evolution of a thermostable esterase. Proc Natl Acad Sci USA 1998;95:12809–12813.
20. Wrba A, Schwaiger A, Schultes V, Jaenicke R, Zavodsky P. Extremely thermostable D-glyceraldehyde-3-phosphate dehydrogenase from eubacterium *Thermotoga maritima*. Biochemistry 1990;29:7585–7592.
21. Zavodsky P, Kardos J, Svingor A, Petsko GA. Adjustment of conformational flexibility is a key event in the thermal adaptation of proteins. Proc Natl Acad Sci USA 1998;95:7406–7411.
22. Chiti F, van Nuland NAJ, Taddei N, Magherini F, Stefani M, Ramponi G, Dobson CM. Conformational stability of muscle acylphosphatase: the role of temperature, denaturant concentration, and pH. Biochemistry 1998;37:1447–1455.
23. van Nuland NAJ, Chiti F, Taddei N, Raugei G, Ramponi G, Dobson CM. Slow folding of muscle acylphosphatase in the absence of intermediates. J Mol Biol 1998;283:883–891.
24. Chiti F, Webster P, Taddei N, Clark A, Stefani M, Ramponi G, Dobson CM. Designing conditions for in vitro formation of amyloid protofilaments and fibrils. Proc Natl Acad Sci USA 1999;96:3590–3594.
25. Taddei N, Chiti F, Paoli P, Fiaschi T, Bucciantini M, Stefani M, Ramponi G, Dobson CM. Thermodynamics and kinetics of folding of common-type acylphosphatase: comparison to the highly homologous muscle isoenzyme. Biochemistry 1999;38:2135–2142.
26. Chiti F, Taddei N, Bucciantini M, White PM, Ramponi G, Dobson CM. Mutational analysis of the propensity for amyloid formation by a globular protein. EMBO J 2000;19:1441–1449.
27. Chiti F, Taddei N, Baroni F, Capanni C, Stefani M, Ramponi G, Dobson CM. Kinetic partitioning of protein folding and aggregation. Nat Struct Biol 2002;9:137–143.
28. Stefani M, Ramponi G. Acylphosphate phosphohydrolases. Life Chem Rep 1995;12:271–301.
29. Degl'Innocenti D, Ramazzotti M, Marzocchini R, Chiti F, Raugei G, Ramponi G. Characterization of a novel *Drosophila melanogaster* acylphosphatase. FEBS Lett 2003;535:171–174.
30. Pastore A, Saudek V, Ramponi G, Williams RJ. Three-dimensional structure of acylphosphatase: refinement and structure analysis. J Mol Biol 1992;224:427–440.
31. Thunnissen MM, Taddei N, Liguri G, Ramponi G, Nordlund P. Crystal structure of common type acylphosphatase from bovine testis. Structure 1997;5:69–79.
32. Zuccotti S, Rosano C, Ramazzotti M, Degl'Innocenti D, Stefani M, Manao G, Bolognesi M. Three-dimensional structural characterization of a novel *Drosophila melanogaster* acylphosphatase. Acta Crystallogr D Biol Crystallogr 2004;60:1177–1179.
33. Bemporad F, Capanni C, Calamai M, Tutino ML, Stefani M, Chiti F. Studying the folding process of the acylphosphatase form *Sulfolobus solfataricus*: a comparative analysis with other proteins from the same superfamily. Biochemistry 2004;43:9116–9126.
34. Plakoutsi G, Stefani M, Taddei N, Chiti F. Aggregation of the acylphosphatase from *Sulfolobus solfataricus*. J Biol Chem 2004; 279:14111–14119.
35. Modesti A, Taddei N, Bucciantini M, Stefani M, Colombini B, Raugei G, Ramponi G. Expression, purification, and characterization of acylphosphatase muscular isoenzyme as fusion protein with glutathione S-transferase. Prot Expr Pur 1995;6:799–805.
36. Ramponi G, Treves C, Guerritore A. Aromatic acyl phosphates as substrates of acyl phosphatase. Arch Biochem Biophys 1966;115: 129–135.
37. Santoro MM, Bolen DW. Unfolding free energy changes determined by the linear extrapolation method 1: unfolding of phenylmethanesulfonyl alpha-chymotrypsin using different denaturants. Biochemistry 1988;27:8063–8068.
38. Braunschweiler L, Ernst RR. Coherence transfer by isotropic mixing: application to proton correlation spectroscopy. J Magn Reson 1983;53:521–528.
39. Piantini U, Sørensen OW, Ernst RR. Multiple quantum filters for elucidating NMR coupling networks. J Am Chem Soc 1982;104: 6800–6801.
40. Jeener J, Meier BH, Bachmann P, Ernst RR. Investigation of exchange processes by two-dimensional NMR spectroscopy. J Chem Phys 1979;71:286–292.
41. Hwang TL, Shaka AJ. Water suppression that works: excitation sculpting using arbitrary waveforms and pulsed field gradients. J Magn Reson 1995;112:275–279.
42. Marion D, Wüthrich K. Application of phase sensitive two-dimensional correlated spectroscopy (COSY) for measurements of proton–proton spin–spin coupling constants in proteins. Biochem Biophys Res Commun 1983;113:967–974.
43. Keeler J, Clowes RT, Davis AL, Laue ED. Pulsed field gradients: theory and practice. Methods Enzymol 1994;239:145–207.
44. Shaka AJ, Lee CJ, Pines A. Iterative schemes for bilinear operators: application to spin decoupling. J Magn Reson 1988;77:274–293.
45. Wüthrich K. NMR spectroscopy of proteins and nucleic acids. New York: Wiley; 1986.
46. Verdone G, Corazza A, Viglino P, Pettirossi F, Giorgetti S, Mangione P, Andreola A, Stoppini M, Bellotti V, Esposito G. The solution structure of human β2-microglobulin reveals the prodromes of its amyloid transition. Protein Sci 2002;11:487–499.
47. Wang Y, Nip AM, Wishart DS. A simple method to quantitatively measure polypeptide $J_{HNH\alpha}$ coupling constants from TOCSY or NOESY spectra. J Biomol NMR 1997;10:373–382.
48. Güntert P, Mumenthaler C, Wüthrich K. Torsion angle dynamics for NMR structure calculation with the new program DYANA. J Mol Biol 1997;273:283–298.
49. Weiner SJ, Kollman PA, Case DA, Singh UC, Ghio C, Alagona G, Profeta S Jr, Weiner P. A new force field for molecular mechanical

simulation of nucleic acids and proteins. J Am Chem Soc 1984;106: 765–784.
50. Esposito G, Fogolari F, Damante G, Formisano S, Tell G, Leonardi A, Di Lauro R, Viglino P. Analysis of the solution structure of the homeodomain of rat thyroid transcription factor 1 by ^{1}H-NMR spectroscopy and restrained molecular mechanics. Eur J Biochem 1996;241:101–113.
51. Doreleijers JF, Rullmann JAC, Kaptein R. Quality assessment of NMR structures: a statistical survey. J Mol Biol 1998;281:149–164.
52. Laskowski RA, Rullmann JAC, MacArthur MW, Kaptein R, Thornton JM. AQUA and PROCHECK-NMR: programs for checking the quality of protein structures solved by NMR. J Biomol NMR 1996;8:477–486.
53. Dayringer HE, Tramontano A, Sprang SR, Fletterick RJ. Interactive program for visualization and modelling of proteins, nucleic acids and small molecules. J Mol Graph 1986;6:82–87.
54. Koradi R, Billeter M, Wüthrich K. MOLMOL: a program for display and analysis of macromolecular structure. J Mol Graph 1996;14:51–55.
55. Kabsh W, Sander C. Dictionary of protein secondary structure: pattern recognition of hydrogen-bonded and geometrical features. Biopolymers 1983;22:2577–2637.
56. Zehfus MH, Rose GD. Compact units in proteins. Biochemistry 1986;23:5759–5765.
57. Vriend G. WHAT IF: a molecular modeling and drug design program. J Mol Graph 1990;8:52–56.
58. Zuccotti S, Rosano C, Bemporad F, Stefani M, Bolognesi M. Preliminary characterization of two different crystal forms of acylphosphatase from the hyperthermophile archaeon *Sulfolobus solfataricus*. Acta Crystallogr 2005;F61:144–146.
59. Navaza J. AmoRE: an automated package for molecular replacement. Acta Crystallogr A 1994;50:157–163.
60. Vagin A, Teplyacov A. An approach to multi-copy search in molecular replacement. Acta Crystallogr D Biol Crystallogr 2000; 56:1622–1624.
61. Storoni LC, McCoy AJ, Read RJ. The likelihood-enhanced fast rotation functions. Acta Crystallogr D Biol Crystallogr 2004;60: 432–438.
62. Murshudov GN, Vagin AA, Dodson EJ. Refinement of macromolecular structures by the maximum-likelihood method. Acta Crystallogr D Biol Crystallogr 1997;53:240–255.
63. Chiti F, Taddei N, White PM, Bucciantini M, Magherini F, Stefani M, Dobson CM. Mutational analysis of acylphosphatase suggests the importance of topology and contact order in protein folding. Nat Struct Biol 1999;6:1005–1009.
64. Vieille C, Zeikus GJ. Hyperthermophilic enzymes: sources, uses, and molecular mechanisms for thermostability. Microbiol Mol Biol Rev 2001;65:1–43.
65. Wilkins DK, Grimshaw SB, Receveur V, Dobson CM, Jones JA, Smith LJ. Hydrodynamic radii of native and denatured proteins measured by pulse field gradient NMR techniques. Biochemistry 1999;38:16424–16431.
66. Taddei N, Stefani M, Vecchi M, Modesti A, Raugei G, Bucciantini M, Magherini F, Ramponi G. Arginine-23 is involved in the catalytic site of muscle acylphosphatase. Biochim Biophys Acta 1994;1208:75–80.
67. Taddei N, Chiti F, Magherini F, Stefani M, Thunnissen MM, Nordlund P, Ramponi G. Structural and kinetic investigations on the 15–21 and 42–45 loops of muscle acylphosphatase: evidence for their involvement in enzyme catalysis and conformational stabilization. Biochemistry 1997;36:7217–7224.
68. Cheung YY, Lam SY, Chu WK, Allen MD, Bycroft M, Wong KB. Crystal structure of a hyperthermophilic archaeal acylphosphatase from *Pyrococcus horikoshii*—structural insights into enzymatic catalysis, thermostability, and dimerization. Biochemistry 2005;44:4601–4611.
69. Stefani M, Taddei N, Ramponi G. Insights into acylphosphatase structure and catalytic mechanism. Cell Mol Life Sci 1997;53:141–151.
70. Rosano C, Zuccotti S, Bucciantini M, Stefani M, Ramponi G, Bolognesi M. Crystal structure and anion binding in the prokaryotic hydrogenase maturation factor HypF acylphosphatase-like domain. J Mol Biol 2002;30:785–796.
71. Chiti F, Taddei N, Stefani M, Dobson CM, Ramponi G. Reduction of the amyloidogenicity of a protein by specific binding of ligands to the native conformation. Protein Sci 2001;10:879–886.
72. Taddei N, Magherini F, Chiti F, Bucciantini M, Raugei G, Stefani M, Ramponi G. C-terminal region contributes to muscle acylphosphatase three-dimensional structure stabilisation. FEBS Lett 1996;384:172–176.
73. Munoz V, Serrano L. Elucidating the folding problem of helical peptides using empirical parameters. Nat Struct Biol 1994;1:399–409.